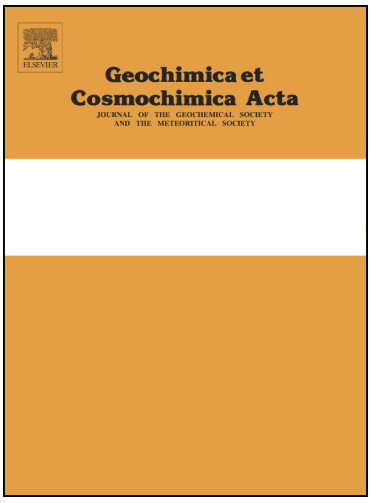

Stable and Clumped Isotope Characterization of Authigenic Carbonates in Methane Cold Seep Environments

Nivedita Thiagarajan, Antoine Crémière, Clara Blättler, Aivo Lepland, Kalle Kirsimäe, John Higgins, Harald Brunstad, John Eiler

PII: S0016-7037(20)30186-1
DOI: https://doi.org/10.1016/j.gca.2020.03.015
Reference: GCA 11692

To appear in: *Geochimica et Cosmochimica Acta*

Received Date: 12 February 2019
Revised Date: 7 March 2020
Accepted Date: 11 March 2020

Please cite this article as: Thiagarajan, N., Crémière, A., Blättler, C., Lepland, A., Kirsimäe, K., Higgins, J., Brunstad, H., Eiler, J., Stable and Clumped Isotope Characterization of Authigenic Carbonates in Methane Cold Seep Environments, *Geochimica et Cosmochimica Acta* (2020), doi: https://doi.org/10.1016/j.gca.2020.03.015

Stable and Clumped Isotope Characterization of Authigenic Carbonates in Methane Cold Seep Environments

Authors: Nivedita Thiagarajan[1*], Antoine Crémière[1], Clara Blättler[2], Aivo Lepland[3], Kalle Kirsimäe[4], John Higgins[5], Harald Brunstad[6], John Eiler[1]

In prep for GCA

Affiliations:

[1]Department of Geological and Planetary Sciences. California Institute of Technology.

[2] Department of the Geophysical Sciences, University of Chicago, Chicago, Illinois 60637, USA

[3]Geological Survey of Norway, 7491 Trondheim, Norway

[4]Department of Geology, University of Tartu, 50411 Tartu, Estonia

[5]Department of Geosciences, Princeton University, Princeton, NJ 08544, USA

[6]Lundin Norway AS, 1366 Lysaker, Norway

.

*Correspondence to: nivedita@caltech.edu

ABSTRACT

Cold seep environments are characterized by methane-rich fluid migration and discharge at the seafloor. These environments are also intimately linked to microbial communities, which oxidize methane anaerobically, increase alkalinity and promote authigenic carbonate precipitation. We have analyzed a suite of methane-derived authigenic carbonate (MDAC) crusts from the North and Barents Sea using stable and clumped isotopes ($\delta^{13}C$, $\delta^{18}O$, $\delta^{44}Ca$, and Δ_{47}) to characterize the sources of fluids as well as the environment of carbonate authigenesis. We additionally assess the potential of MDACs as a Δ_{47}-based paleotemperature archive.

The MDACs occur as three main textural-mineralogic types: micritic Mg-calcite cements, micritic aragonite cements and cavity filling aragonite cements. We find that micritic Mg-calcite cements have low $\delta^{13}C_{PDB}$ values (-30 to -47‰), high $\delta^{44}Ca$ values (-0.4 to -0.8‰), and Δ_{47}-temperatures (0-6 °C) consistent with shallow sub-seafloor precipitation in isotopic equilibrium. Micritic aragonite cements and cavity filling aragonite cements both have a wider range in $\delta^{13}C_{PDB}$ values (-18 to -58‰), lower $\delta^{44}Ca$ values (-0.8 to -1.6‰) and a larger range in Δ_{47}-based apparent temperatures (0-25 °C) with most but not all samples consistent with clumped isotopic equilibrium.

The range in apparent temperatures as well as $\delta^{44}Ca$ values seen in the aragonite MDACs suggest two kinetic processes: a kinetic isotope effect (KIE) due to the incomplete equilibration of carbon and oxygen isotopes among DIC species from the different sources of DIC (i.e., seawater, methane-sourced DIC and DIC residual to CO_2 degassing or diffusion) and a KIE due to a fast, irreversible precipitation affecting the cations, particularly Ca, bound to carbonate mineral. Our results improve the understanding of kinetic effects on clumped isotope

temperatures in MDACs and demonstrate how the multi-isotopic approach combined with textural-mineralogic criteria can be used to identify MDACs for accurate paleotemperature reconstructions.

1. INTRODUCTION

Authigenic carbonate precipitates forming at cold seep environments in response to the migration of methane-rich fluids through the sediment column are a relatively new archive for learning about regional environmental conditions (Aloisi et al., 2002; Bayon et al., 2013; Crémière et al., 2016b; Cui et al., 2017). However, understanding their chemical and isotopic signatures requires first addressing the complex biogeochemical processes that form these precipitates. The carbonate precipitates are predominantly found at oceanic margins with areas of active seepage often linked to offshore hydrocarbon reservoirs (Kvenvolden, 1993; Suess, 2014). The methane-rich fluids promote the activity of chemosynthetic biological communities and the dominant biogeochemical process is sulfate-driven anaerobic oxidation of methane (AOM). AOM consumes a significant proportion of the methane rising to the seabed, and thus represents the main methane sink in marine sediments (Reeburgh, 2007). AOM is controlled by a consortium of methane-oxidizing archaea and sulfate reducing bacteria (Boetius et al., 2000; McGlynn et al., 2015). Elevated carbonate alkalinity as a result of AOM in the shallow subsurface promotes the precipitation of methane-derived authigenic carbonates (MDAC), which constitute unique archives of the biogeochemical processes associated with the migration of methane rich fluids.

Stable carbon and oxygen isotopes have been applied to MDACs to provide information on fluid source and environmental conditions during carbonate formation (Bohrmann et al., 1998; Han et al., 2004). Notably, MDACs are characterized by strongly negative $\delta^{13}C$ values, which reflect the influence of methane-derived dissolved inorganic carbon (DIC), a by-product of AOM across the sulfate-methane transition zone (SMTZ) in marine sediments. The degree of ^{13}C depletion may provide a means to indirectly trace fluid sources, and to differentiate between microbial methane ($\delta^{13}C$ from −120 to −45‰ VPDB) and thermogenic methane ($\delta^{13}C$ from −50 to −20‰ VPDB) (Whiticar, 1999). Oxygen isotopes have been more difficult to interpret as there are two different fluid sources with variable $\delta^{18}O$ for the carbonate precipitation environment: seawater, and porewaters. The oxygen isotopic composition of these two different fluids can additionally be altered by various processes including clathrate formation and dissociation, clay mineral dehydration and the input of continental ground waters. Therefore, using the $\delta^{18}O$ of the MDACs to reconstruct bottom water temperature is complicated due to the difficulty in accurately assuming the $\delta^{18}O$ of the precipitation environment water and how it changed with time.

Carbonate clumped isotope thermometry is a relatively new temperature proxy based on the ordering of ^{13}C and ^{18}O atoms into bonds with each other in the same carbonate molecule (Ghosh et al., 2006; Eiler, 2011). The excess of bonds between ^{13}C and ^{18}O in a carbonate mineral, relative to those that would arise by random chance, has an inverse relationship with growth temperature. This isotopic ‘clumping’ phenomenon exists due to a thermodynamically controlled homogeneous isotope exchange equilibrium in the carbonate mineral. The exchange reaction is independent of the $\delta^{18}O$ of water and $\delta^{13}C$ of DIC from which the carbonates precipitate; therefore it can be applied to settings where these quantities are not known (Eiler, 2011).

Clumped isotopes have previously been investigated in MDACs and were found to exhibit equilibrium temperatures (Wacker et al., 2014; Zhang et al., 2019) as well as anomalously low clumped signatures (or hot apparent clumped isotope temperatures) (Loyd et al., 2016). Although various kinetic isotope effects were proposed to explain the observed disequilibra (methane oxidation, mixing of inorganic carbon pools, pH and precipitation rates), no predictive mechanism was proposed to explain the isotope signatures. Additionally, recent work (Schauer et al., 2016; Daëron et al., 2016) has shown that previous clumped isotope measurements made on samples having bulk $\delta^{13}C$ and/or $\delta^{18}O$ values several tens of per mil different from the reference CO_2 used as a mass spectrometric standard, suffer from systematic errors in inferred temperature, of several degrees or more, as a result of an error in the estimated abundance of ^{17}O in Standard Mean Ocean Water. Here we extend the previous clumped isotope MDAC studies (Wacker et al., 2014; Loyd et al., 2016; Zhang et al., 2019) and analyze the different textural-mineralogic carbonate types found in the North Sea and Barents Sea MDAC crusts. We process the clumped isotope data using the updated ^{17}O content of SMOW (Brand et al., 2010) and also provide Ca isotope data and trace metal concentrations of our MDAC samples which provide an additional indication of kinetic isotope effects associated with carbonate precipitation (Lemarchand et al., 2004; Tang et al., 2012; Nielsen et al., 2012; Gabitov et al., 2014).

We have several goals with this study. Our first and main goal is to determine how MDACs form and whether we can use various chemical signatures to reconstruct past environments. Second, we will characterize the precipitation environment and assess the proportions of methane-derived bicarbonate, ocean dissolved inorganic carbon and clathrate derived pore water to the calcifying medium used to precipitate MDACs. Third, we will investigate how changes in DIC chemistry, including pH, CO_2 hydration, hydroxylation and solvation affect carbonate growth. And finally, we will explore if there are kinetic isotope effects associated with mineral growth of different phase of carbonate, including metastable aragonite and the more stable Mg-calcite.

2. MATERIALS AND METHODS

2.1 Samples

Studied MDAC crusts were collected from the Barents and North Sea via remotely operated vehicle (ROV), and have previously been analyzed for U-Th ages, stable carbon and oxygen isotope composition as well as trace metals (Crémière et al., 2016a; Crémière et al., 2016b). The MDACs were found in bottom water temperatures estimated to range from 5-6°C in the North Sea and 2-3°C in the Barents Sea based on the World Ocean Atlas 2018 database. The recovered MDAC crusts are typically 10-30 cm thick and contain three textural-mineralogic carbonate types: micritic Mg-calcite cement, micritic aragonite cement and cavity filling aragonite cement (Crémière et al., 2016b). The two micritic cements lithify the host sediment, typically mud and sand size detrital material and represent early generation carbonate precipitates. These early generation Mg-calcite and aragonite cemented sediments contain cavities that are thought to be conduits generated by a focused fluid flow that washes out unlithified sediments. Late generation cavity filling aragonite cements precipitate in the cavities and form detritus-free, translucent, botryoidal layers up to 10 mm thick. Rare earth element (Crémière et al., 2016b) and geologic evidence (Aloisi et al., 2002) suggests that micritic Mg-calcite cements typically precipitate deeper in the sediment column under lower methane flux,

while the micritic aragonite cements form under higher methane flux close to the sediment-water interface.

We sampled ten individual MDAC crusts with ages ranging from 2000-16,000 years to perform our clumped isotope characterization. MDAC crusts were cut and polished slabs and thick-sections were made and studied under optical and scanning electron microscope for petrographic characterization and selection of sampling areas. Up to six samples were microdrilled from studied MDAC crusts with a diamond cutting dental bit with a diameter of ~1 mm targeting a single petrographic-mineralogic type at a time (micritic aragonite cement, micritic Mg-calcite cement or aragonite cavity filling cement). Splits of the same microdrilled samples were made for clumped isotope, X-ray diffraction (XRD) mineralogy and Ca isotope analysis.

2.2 Δ_{47} Analysis:

Samples were analyzed for Δ_{47} using previously established methods (Ghosh et al., 2006; Huntington et al., 2009; Passey et al., 2010; Dennis and Schrag, 2010). Briefly, 8 mg of samples were drilled from thick sections and digested with phosphoric acid at 90^{o}C to produce CO_2. The CO_2 was separated from H_2O using a dry ice/ethanol trap. The CO_2 was further purified from trace organics and other polar contaminants by entraining it in He and passing over a Porapak Q 120/80 mesh column held at -20 °C. The resulting CO_2 was again purified from He using dry ice/ethanol and nitrogen traps and expanded into the bellows of the mass spectrometer. The evolved CO_2 was analyzed in a dual inlet Finnigan MAT-253 mass spectrometer with the simultaneous collection of ion beams corresponding to masses 44-49 to obtain Δ_{47}, Δ_{48}, $\delta^{13}C$ and $\delta^{18}O$ values. Masses 44-46 are registered through $3*10^8$ to $10^{11}\Omega$ resistors while masses 47 and 48 are registered through 10^{12} Ω resistors. The mass 47 beam is composed of $^{17}O^{13}C^{17}O$, $^{17}O^{12}C^{18}O$ and predominantly $^{18}O^{13}C^{16}O$ and we define R^{47} as the abundance of mass 47 isotopologues divided by the mass 44 isotopologue. ($R^{47} = [^{17}O^{13}C^{17}O + {}^{17}O^{12}C^{18}O + {}^{18}O^{13}C^{16}O]/[{}^{16}O^{12}C^{16}O]$.) Δ_{47} is reported relative to a stochastic distribution of isotopologues for the same bulk isotopic composition. ($\Delta_{47} = (((R^{47}_{measured}/R^{47}_{stochastic})-1) - ((R^{46}_{measured}/R^{46}_{stochastic})-1) - ((R^{45}_{measured}/R^{45}_{stochastic})-1))*1000$.) Mass 48 was monitored to detect any hydrocarbon contamination. Each measurement of an unknown sample was evaluated for possible contamination based on its location in a plot of 'raw' (non-heated-gas-corrected) Δ_{48} vs. 'raw' (vs. the working gas) δ_{48}. If the sample falls within 3σ standard deviation (where the standard deviation is based on the internal statistics of the analysis of that sample) of the average trend in that plot for heated gases analyzed during the same analytical session, then it is judged to present no positive evidence for hydrocarbon contamination. Samples that do not meet this criterion (i.e., fall more than 3σ SD from the line) are judged to be contaminated. All measured samples fell on the Δ_{48}-line derived from heated and equilibrated gases within 3σ. Measurements of each gas were done at 16 V of mass 44 and consisted of 8 acquisitions, each of which involved 7 cycles of sample-standard comparison with an ion integration time of 26 s per cycle. The average of our internal standard errors is 0.016‰ and our pooled standard deviation of our 3 standards (CIT Carrara Marble, TV04 and a deep sea coral standard, LB002) is 0.018‰. We report two types of errors. In the supplementary table we report the 1σ propagated errors of the internal error, heated gas line error and Δ_{47}-temperature calibration. On our figures we plot our data with the pooled standard deviation of 3 of our standards, CIT Carrara Marble, TV04 and a deep sea coral standard, LB002.

$\delta^{13}C_{VPDB}$ and $\delta^{18}O_{VSMOW}$ values of samples and standards were calculated from raw ion currents on masses 44, 45, and 46 of sample and working gases using the "Brand" parameters reported in Brand et al. (2010). The acid digestion fractionation factors for aragonite and calcite have been calculated between 25 to 75 °C, and we extrapolate these values to 90 °C and use them in our calculations (Kim et al., 2007a). The aragonite acid digestion fractionation factor was used for aragonite minerals while the calcite digestion fractionation factor was used for Mg-calcite. Previous work has characterized the Mg-calcite having a Mg mol % of around 10-20 (Crémière et al., 2016). Given the very small sample amounts of our drilled samples, we were not able to use XRD to quantify Mg abundance in the Mg-calcite. Using the values in (Tarutani et al., 1969), a 20 Mg mol % would alter the $\delta^{18}O$ value by 1.2‰. Raw Δ_{47} values were then calculated from the difference in R^{47} relative to the reference gas and the newly derived $\delta^{13}C_{VPDB}$ and $\delta^{18}O_{VSMOW}$ values of the derived sample gas. The Δ_{47} raw data was corrected for instrument nonlinearity and scale compression (Huntington et al., 2009; Passey et al., 2010). Several heated and equilibrated gases of various bulk isotopic compositions were run during each session. These gases were used to convert measurements into the interlaboratory absolute reference frame (Dennis et al., 2011).

2.2.1 Δ_{47}-Temperature Calibration:

We converted Δ_{47ARF} into temperature using a new calibration consisting of two previous calibrations (Ghosh et al., 2006; Thiagarajan et al., 2011). We combine these two calibrations as they together contain more than 20 points above Δ_{47} = 0.75‰, where most of our measurements fall. We do not use a previously published interlab calibration (Bonifacie et al., 2017), as it does not include inorganic calibration points of low temperatures (high Δ_{47} values) from labs with a "steep slope." Among various carbonate clumped isotope labs, there are two general families of Δ_{47}-temperature calibration lines, one with a "steep-slope" and another with a "shallow-slope." These two types of calibrations are similar in slope among different labs at temperatures above 20 °C, but are markedly different at temperatures below 20 °C. Despite substantial effort by the clumped isotope community, no explanation has been found to explain the difference in the slopes of the calibration between different labs (Bonifacie et al., 2017). The Bonifacie et al., 2017 compilation has been found to be suited for carbonate minerals from -1 to 300 °C; however, the low temperature (T <20 °C) calibration points used in their compilation come from labs that produce "shallow slope" calibrations lines. The Caltech clumped isotope lab consistently produces calibration lines with steeper slopes (Ghosh et al., 2006; Tripati et al., 2010; Thiagarajan et al., 2011; Eagle et al., 2013; Hines et al., 2019). Additionally, the slowest growth inorganic calcite in an inorganic calcite experiment show that Δ_{47} values are consistent with the steep slope Δ_{47}-temperature calibration of Ghosh et al 2006 (see Figure 6 and 7 in (Levitt et al., 2018)). We use two "steep-slope" calibrations (Ghosh et al., 2006; Thiagarajan et al., 2011) updated into the absolute reference frame to correct our data. The equation of the new calibration is $\Delta_{47} = (63015 \pm 0.3630) / T^2 - 0.0015 \pm 0.0045$ with an R^2=0.93.

2.3 XRD Analysis:

The mineralogical composition of samples was studied by means of X-ray diffractometry (XRD). Samples were pulverized by hand with an agate pestle and mortar under ethanol and preparations were made by dropping sample suspension on low-background Si wafers. Dried preparations were scanned on a Bruker D8 Advance using Cu*K*α radiation and LynxEye positive sensitive detector in 2–70° 2Θ range with step size 0.012° and counting time 1 s per step. The

semi-quantitative mineralogical composition of the samples was interpreted and modelled using the Rietveld algorithm-based code Topaz by Bruker. The relative error of quantification is better than 10% for major phases (>5 wt%) and better than 20% for minor phases (<5 wt%).

2.4 Ca isotopes and Trace Element Ratios

Calcium isotope ratios were measured at Princeton University. One to four milligrams of samples were dissolved in 0.2% nitric acid and left standing for any insoluble material to settle. The dissolved phase was then diluted to approximately 30 ppm calcium and the calcium ions were separated from other cations with an automated ion chromatography system (Thermo-Dionex ICS-5000^{+}). These purified samples of calcium were dried down, treated with 200 µL of distilled concentrated nitric acid, dried down again, and then redissolved in 2% nitric acid to a concentration of 2 ppm calcium. Isotopic ratios of calcium were analyzed in these solutions with a Thermo Neptune Plus multi-collector inductively coupled plasma mass spectrometer (ICP-MS) with an ESI Apex-IR sample introduction system. Corrections for isobaric strontium interferences were based on the double-charged ^{87}Sr peak; polyatomic interferences (e.g. $^{40}ArHH^{+}$) were avoided with sufficient mass resolution. Sample-standard bracketing was used to calculate $\delta^{44/40}Ca$ values relative to modern seawater. A triple-isotope plot shows the expected mass dependence among ^{44}Ca, ^{43}Ca, and ^{42}Ca. Reported $\delta^{44/40}Ca$ values are calculated following kinetic fractionation laws (Young et al., 2002) and assuming no radiogenic ^{40}Ca excess, which is consistent with previous work showing a lack of resolvable ^{40}Ca excess in modern seawater (Caro et al., 2010). External precision on $\delta^{44/40}Ca$ values is ± 0.14‰ (2σ), derived from the long-term reproducibility of the carbonate standard SRM-915b treated as an unknown sample (n = 155). The $\delta^{44/40}Ca$ value obtained for SRM-915b is –1.15‰, which is indistinguishable from published values (Heuser and Eisenhauer, 2008).

Trace elements were analyzed in the same initial solutions using a quadrupole ICP-MS at Princeton University (Thermo iCAP). Samples were diluted to approximately 10 ppm calcium, and scandium was added as an internal standard. External standard calibration curves bracketed the concentrations of each element of interest in the sample solutions, yielding precision of approximately ± 5%. Trace element concentrations are normalized to that of calcium and reported as molar ratios.

3. RESULTS

The carbonate phases in studied MDAC crust samples are dominated by authigenic Mg-calcite and aragonite with minor detrital dolomite and calcite (mainly biogenic debris) as determined by petrographic observations and XRD analysis (Figure 2). Aragonite occurs dominantly as cryptocrystalline and/or radial fibrous aggregates forming botryoidal linings on cavity walls (Figure2a, SI Figure 1), or microcrystalline aragonite cement in sand-sized detrital sediments (Figure 2b). Mg-calcite occurs as micritic cement in sandy mud (Figure 2c). Table 1-4, Figure 3 and 4 summarize the results of all isotopic analyses. The North Sea samples have $\delta^{13}C_{PDB}$ values ranging from -58 to -46‰, $\delta^{18}O_{PDB}$ values ranging from 2.2 to 3.5‰ and clumped isotope apparent temperatures ranging from 3 to 24°C (Figure 4). The Barents Sea samples have a larger spread of $\delta^{13}C$ values ranging from -43 to -18‰, $\delta^{18}O_{PDB}$ values ranging from 3.3 to 5.4‰ and apparent Δ_{47}-temperatures ranging from -1 to 22°C (Figure 3).

Based on microscopic observations, paragenetic relationships and mineralogical composition we have subdivided the isotopic data into the three distinct textural-mineralogical groups. Each subgroup bears distinct isotopic signatures. Both in the Barents and North Sea

MDAC crusts, micritic Mg-calcite cements record clumped isotope apparent temperatures consistent with independently known bottom water temperatures within 2σ errors. In the Barents Sea, all but one micritic aragonite cement also record bottom water temperatures; however, in the North Sea none of the micritic aragonite cements record bottom water temperatures. Eight out of the nineteen cavity filling micritic aragonite cements from the Barents Sea yield Δ_{47} values consistent with bottom water temperatures, while the other eleven yield temperatures several degrees warmer than bottom water. At the North Sea, all cavity filling aragonite cements yield temperatures warmer than bottom water.

The $\delta^{18}O$ and clumped isotope apparent temperature relationships for cavity filling aragonite cement have an unusual and noteworthy feature: A plot of temperature vs $\delta^{18}O$ of the Barents Sea cavity filling aragonite cements reveals a kink or "V" structure to the data set (Figure 4a). This "V" is not seen in plots of temperature vs $\delta^{13}C$ (Figure 4b). In addition, the cavity filling aragonite cement displays a trend in $\delta^{13}C$ where the Δ_{47}–temperature deviation from bottom water temperature increases with decreasing $\delta^{13}C$ values (Figure 4b).

The $\delta^{44}Ca$ values show a wide range, separated to first order by the mineralogy of the samples. The Mg-calcite $\delta^{44}Ca$ values in the Barents Sea and North Sea range from -0.3 to -0.7‰ in the Barents and North Sea, while the $\delta^{44}Ca$ for micritic aragonite cement and cavity filling aragonite cement range from -0.5 to -1.5‰ in the Barents Sea and -0.7 to -1.4‰ in the North Sea (Fig. 5). Sr/Ca ratios range from 6-14 mmol/mol for the aragonite and 1 to 11 mmol/mol for high Mg-calcite samples. The cavity filling aragonite cements exhibit approximately linear trends in plots of clumped isotope apparent temperature vs $\delta^{44}Ca$ and $\delta^{13}C$ vs $\delta^{44}Ca$, while the micritic aragonite cement only shows a linear trend in the latter of these two plots. Additionally, the Mg-calcite and aragonite have non-overlapping $\delta^{44}Ca$ and Sr/Ca ratios, with one exception. In contrast, the two petrographically distinct aragonite populations have overlapping $\delta^{44}Ca$ and Sr/Ca values.

4. DISCUSSION

4.1 Relationship of Δ_{47} to environmental temperature and kinetic isotope effects

The clumped isotopic compositions of the MDACs have a varied response to temperature of the precipitation environment but there are some clear and systematic patterns. The micritic Mg-calcite cements in both the North Sea and Barents Sea record bottom water temperatures within 2σ error bars. On the other hand, both micritic and cavity filling varieties of aragonite have a more complicated relationship to temperature. In the Barents Sea, micritic aragonite cements record bottom water temperature while in the North Sea they do not and yield much warmer apparent temperatures. Additionally, the cavity filling aragonite cements in both locations record a range of apparent temperatures from bottom water temperatures to ~22°C.

Given that MDACs exhibit kinetic isotope effects in one or more isotopic systems, we explore various mechanisms purported to cause disequilibrium signatures in the aragonites. In this section we focus on carbon, oxygen and clumped isotopes, to be followed by additional context provided by the $\delta^{44}Ca$ and Sr/Ca values. To illustrate this discussion, we make a plot of $\Delta_{47,measured}$- $\Delta_{47,expected}$ versus $\delta^{18}O_{measured}$- $\delta^{18}O_{expected}$ (Figure 6) with the MDAC crusts that have been U/Th dated (Crémière et al., 2016a; Crémière et al., 2016b). For Holocene samples, we use modern values of temperature and our new Δ_{47} calibration to temperature to calculate $\Delta_{47,expected}$. For deglacial, late Pleistocene samples (11.7-16 kya), we use estimates of bottom water

temperatures of 2-6 °C as determined from $\delta^{18}O$ of benthic foraminifera in core JM05-085-GC collected in the SW Barents Sea basin (Aagaard-Sørensen et al., 2010), and our new Δ_{47} calibration to temperature to calculate $\Delta_{47,expected}$. The larger ranges in late Pleistocene bottom water temperature result in significantly larger vertical error bars on late Pleistocene MDACs compared to the Holocene MDACs in Figure 6. To calculate the Holocene $\delta^{18}O_{expected}$, we use modern bottom water temperatures, a relatively generous estimate of $\delta^{18}O_{water}$ of 0 to 3‰ and the previously published $\delta^{18}O$ calibrations for the fractionation between calcite (or aragonite) and water (Kim and O'Neil, 1997; Kim et al., 2007b). We use this large range in $\delta^{18}O_{water}$ as the MDACs may experience several different types of water, including seawater, light $\delta^{18}O$ continental freshwater and heavy clathrate derived pore water, therefore it is difficult to know precisely what the $\delta^{18}O$ of the water of the calcifying fluid was, even for modern MDACs. To calculate the late Pleistocene $\delta^{18}O_{expected}$, we use the late Pleistocene bottom water estimate as well as the same range in $\delta^{18}O_{water}$ of 0-3‰. By comparing the measured Δ_{47} and $\delta^{18}O$ values with the expected values, we can test for the plausibility of various mechanisms to explain the observed isotopic behavior in the MDACs, including mixing effects, diffusion, hydration and dehydroxylation, rate and pH.

4.1.1 Mixing

We first investigate changes in mixing to explain stable and clumped isotope patterns as MDACs form from multiple fluid sources including DIC produced by AOM, DIC from seawater and clathrate derived pore fluids, each of which have very distinct isotopic compositions. Based on previously reported methane data (Crémière et al., 2016a; Crémière et al., 2016b; Crémière et al., 2018) and accounting for the fractionation during AOM we estimate that DIC produced by AOM has a $\delta^{13}C$ value of -45‰ in the Barents Sea study area (indicative of methane derived from a predominantly thermogenic source) and -75‰ in the North Sea study area (indicative of methane derived from a microbial source). DIC in seawater typically has a $\delta^{13}C$ of 0‰ and a $\delta^{18}O$ of 1‰, while water incorporated in the matrix of clathrates tend to have heavy $\delta^{18}O$ values as high as 3‰ (Davidson et al., 1983). The stable carbon and oxygen isotopes of MDACs from both the Barents Sea and North Sea have previously been noted to be consistent with precipitating from a mixture of these fluids with variable proportions (Crémière et al., 2016b).

Mixing relationships in clumped isotopes have been studied by a number of authors and these studies have found that mixing two different populations of CO_2 , HCO_3^- and CO_3^{2-} causes strong disequilibrium clumped isotope signatures in the resultant mixtures (Defliese and Lohmann, 2015; Eiler and Schauble, 2004). This disequilibrium signature is due to the subtle curvature in the stochastic distribution of mass-47 isotopologues seen in a 3D plot of $\delta^{13}C$ vs., $\delta^{18}O$ vs. R^{47} (Eiler and Schauble, 2004). Due to this curvature, conservative mixing of two CO_2, HCO_3^- or CO_3^- populations that have the same Δ_{47} but different $\delta^{13}C$ and $\delta^{18}O$ values leads to a mixed population having a Δ_{47} value different than the endmembers. The maximum offset from the endmembers generally occurs at 50:50 mixture of the two sources.

We calculate offsets expected from mixtures of DIC produced by complete oxidation of methane in the Barents Sea ($\delta^{13}C_{CO32-}$ = -45‰, $\delta^{18}O_{water, SMOW}$ = 2‰, temperature = 3 °C) with seawater ($\delta^{13}C_{CO32-}$=1‰, $\delta^{18}O_{water, SMOW}$ = 0‰, temperature = 3 °C) as well as mixtures of DIC produced by complete oxidation of methane in the North Sea ($\delta^{13}C_{CO32-}$=-75‰, $\delta^{18}O_{water, SMOW}$ = 2‰, temperature = 6 °C) with a seawater ($\delta^{13}C_{CO32-}$=1‰, $\delta^{18}O_{water, SMOW}$ = 0‰, temperature = 6 °C). We first calculate Δ_{63} values of CO_3^{2-} (i.e., enrichment in mass-63 carbonate ion

isotopologues, analogous to the Δ_{47} values of CO_2) that would be produced in equilibrium with CO_2 derived from AOM and calculate the mixing effect on Δ_{63} that would be seen when the AOM-derived CO_3^{2-} is mixed with variable proportions of seawater. We then convert this Δ_{63} to a Δ_{47} value that would be seen in the MDACs produced in equilibrium with the mixed DIC. We find that mixing produces a range in $\delta^{18}O$ of carbonate of 2‰ and apparent Δ_{47}-temperatures up to 5 °C higher than bottom water temperatures. Figure 6 shows that some of the variability seen in the cavity filling aragonite cements can be explained by mixing effects, however most of the warm Δ_{47}-apparent temperatures above 10 °C (more negative $\Delta_{47measured}$-$\Delta_{47expected}$ values) cannot be explained by mixtures of DIC derived from AOM and seawater.

4.1.2 Diffusion

Diffusion of AOM derived CO_2 in the sediments could conceivably cause the nonequilibrium signatures that we observe in the studied samples. We do not have a mechanistic understanding of how diffusion of CO_2 through pore fluids might affect the Δ_{47} value, however, we can use other types of diffusion to make inferences. The kinetic theory of gases provides some guidance to the mass dependence of diffusion controlled isotopic fractionations. Knudsen diffusion (diffusion of gas through a small aperture) predicts that for a CO_2 population that has undergone diffusive fractionation, the isotopic composition of the diffused gas, compared to the starting composition, will decrease on a trend of $\delta^{13}C$ and $\delta^{18}O$ by 11.2‰ and 22.2‰, respectively and increase Δ_{47} by 0.5‰ as diffusion continues to progress (Eiler and Schauble, 2004). Similarly, gas phase inter-diffusion of CO_2 through air (i.e., where collisions between CO_2 and other molecules influences the diffusion rate) generates fractionations of -4.4‰ for $\delta^{13}C$, -8.7‰ for $\delta^{18}O$ and +0.3‰ for Δ_{47} compared to the starting composition (Eiler and Schauble, 2004). In both cases, the increase in Δ_{47} is due to the difference between the diffusive mass law and the dependence of stochastic abundances of mass-47 CO_2 isotopologues on bulk isotopic composition (Eiler and Schauble, 2004). The residues of diffused gas populations have similar amplitude isotopic signatures as the diffused gas population but opposite in sign (i.e., for the case of inter-diffusion, high $\delta^{13}C$ and $\delta^{18}O$ and increased Δ_{47}-temperatures compared to the starting composition).

Isotopic fractionations caused by diffusion of molecules in liquids are generally smaller than diffusion in gases (O'Leary, 1984). If MDAC precipitation is dominated by the residues of CO_2 diffusion in porewaters, we predict fractionations will be even smaller than what is observed for the residues of gas phase diffusion, but regardless the diffused population of gases will have a higher $\delta^{13}C$ and $\delta^{18}O$ than expected and the Δ_{47}-temperature will be warmer than expected. As a portion of Δ_{47} and $\delta^{18}O$ data falls along vectors consistent with the residues of a diffused gas sample, we believe diffusion of CO_2 from subsurface locations where AOM is occurring to the sediment seafloor interface plays a role in MDAC formation (Figure 6).

4.1.3 CO_2 dehydroxylation and dehydration

Degassing of CO_2 from aqueous solutions proceeds through bicarbonate dehydration ($H^+ + HCO_3^-{}_{(aq)} \rightarrow H_2CO_3 \rightarrow CO_2 + H_2O$) and bicarbonate dehydroxylation ($HCO_3^-{}_{(aq)} \rightarrow CO_2 + OH^-$). CO_2 degassing has previously been suggested to occur in methane seep environments and is tied to high methane concentrations (Römer et al., 2012; Smrzka et al., 2015). The amount of methane in subsurface environment is controlled by the flux of methane delivered and the efficiency of microorganisms to oxidize methane. In certain high methane flux environments, if the methane flux outstrips the capability to oxidize methane, methane can escape into the water

column and when CO_2 is supersaturated in solution, it is also degassed along with the methane. Previous work has reported up to 0.7 mol% CO_2 in gas phase from high gas flux methane seep environments (Römer et al., 2012; Crémière et al., 2016a; Crémière et al., 2018). Theoretical calculations of the kinetic isotope effects on carbonates formed from a DIC solution where CO_2 has been degassed have found that the Δ_{47} of carbonates formed from the resultant fluid would decrease by 0.01–0.05‰ (increase Δ_{47}-temperature by 2-10 °C) for every 1‰ decrease in $\delta^{18}O$ (Falk et al., 2016) compared to carbonates that had formed in a similar fluid with no CO_2 degassing. The overlap of some of the MDAC data with CO_2 dehydration and dehydroxylation vectors suggests that CO_2 degassing plays a role in lowering the Δ_{47} values in DIC (Figure 6) and under certain precipitation conditions that low Δ_{47} (warm Δ_{47}-temperatures) is recorded in the aragonite MDACs.

4.1.4 pH, DIC equilibration pH, and rate of precipitation

The rate of DIC equilibration plays a crucial role in setting the oxygen and clumped isotope composition of fast precipitating carbonates. In systems with multiple sources of DIC, such as the methane seep system, dissolved CO_2 is crucial for the oxygen isotope equilibration in DIC because the direct exchange of oxygen isotopes between DIC and H_2O is only possible via the CO_2 hydration and CO_2 hydroxylation reaction (e.g., Zeebe and Wolf-Gladrow, 2001). Therefore, the rate of uncatalyzed oxygen isotope exchange is determined by the kinetic rate constants for the CO_2 hydration and hydroxylation as well as the DIC speciation, which is a function of pH. At seawater conditions (T=19 °C, S=35, pH 8), the time for 99% oxygen equilibration is ~750 minutes (Wolf-Gladrow and Zeebe, 2001). In natural settings, it is possible that the DIC species are isotopically equilibrated with water owing to the presence of the enzyme carbonic anhydrase (CA), which promotes rapid exchange of oxygen isotopes in aqueous solution by enhancing the rate of CO_2 hydration and can reduce the timescale of equilibration by a factor of 2 or more (Uchikawa and Zeebe, 2012). We are not aware of any measurements of the activity of carbonic anhydrase in sediments in the Barents or North Sea. Therefore, carbonates which precipitate from a solution where the residence time of DIC species in solution is longer than ~10^2-10^3 minutes, will precipitate from a solution that is not at oxygen isotopic equilibrium and therefore will not record an equilibrium signature.

The rate of carbonate precipitation can additionally affect the isotopic composition of the precipitating carbonate. The role of growth rate on oxygen isotopes is not straightforward. Previous work has shown that the measured oxygen isotopic fractionation of carbonates may vary depending on the rate of precipitation (McConnaughey, 1989; Watkins and Hunt, 2015; Staudigel and Swart, 2018) or may also be independent of precipitation rate (Tarutani et al., 1969; Kim and O'Neil, 1997). Similarly for clumped isotopes, an ion-by-ion growth model predicts there to be a rate dependent kinetic isotope effect on clumped isotopes (Watkins and Hunt, 2015), while observations of inorganic laboratory calcite indicate that Δ_{47} is independent of precipitation rate (Tang et al., 2014; Levitt et al., 2018). Disentangling the effects of carbonate precipitation rate on oxygen and clumped isotopes is beyond the scope of our study but is a promising line of future research.

Variations in pH have been shown to affect the oxygen and carbon isotope composition of inorganically precipitated carbonates (McRea, 1950; Usdowski et al., 1991). This observation has been explained by the pH dependent speciation of the DIC pool from which carbonate precipitates and the different fractionation factors between water and these DIC species. At seawater-like pHs, HCO_3^- dominates whereas at high pHs, CO_3^{2-} dominates the DIC. Previous

work has shown that the oxygen isotopic composition of the solid precipitated from solution reflects the weighted average of all the fractionation factors with respect to water for all the carbonate species (Zeebe, 1999). This effect has been used to explain variations seen in oxygen isotopes in inorganic calcite calibration experiments and stable oxygen isotope ratios of foraminiferal calcite (Zeebe, 1999). Although some work has suggested that CO_3^{2-} is the dominant DIC species contributing to carbonate formation and that HCO_3^- only plays a minor role in carbonate growth (Kim et al., 2006; Devriendt et al., 2017), we assume that HCO_3^- and CO_3^{2-} both contribute to carbonate formation in proportion to their abundance in DIC (Zeebe, 1999; Watkins and Hunt, 2015). Future work could clarify the role that HCO_3^- plays in the precipitation of carbonates.

Watkins and Hunt (2015) developed a model that calculates the oxygen, carbon, and clumped isotope composition of calcite as a function of temperature, crystal growth rate, and solution pH. We use this model to calculate the expected carbon, oxygen and clumped isotope fractionation for bottom water conditions (temperature = 6 °C, salinity = 35‰, $[Ca^{2+}]$ = 10 mol/kg) at a range of precipitation rates (1-4000 nmol cm^2/day) (Loyd et al., 2016) and pHs (7-8) the MDACs are thought to experience. We find that when pH and precipitation rates are at the highest values, i.e. the conditions that should offer the maximum offset from equilibrium, the clumped isotope apparent temperatures only reach 11 °C. As the Δ_{47}-temperatures seen in the MDACs reach values as high as 22 °C, we conclude that variations in precipitation and rate can explain some of the observed offset but not all of it.

Our analysis of mechanisms in conjunction with the plot of $\Delta_{47,measured}$- $\Delta_{47,expected}$ versus $\delta^{18}O_{measured}$- $\delta^{18}O_{expected}$ indicates that there are several physical mechanisms that plausibly could be consistent with the isotopic data including mixing, diffusive escape, CO_2 dehydration and dehydroxylation, pH changes and precipitation rate. No single mechanism can explain the full range seen, but it is possible that several of these effects occur simultaneously and are contributing to the observed isotopic signals.

4.2 Behavior of Calcium Isotopes and Sr/Ca

Taking the above insights from carbon and oxygen isotopes, we can explore if the mechanisms used to explain their variations are consistent with the behavior of the cation component of calcite and aragonite minerals, which are known to exhibit kinetic effects. The largely non-overlapping nature of calcium isotope ratios and Sr/Ca data between the Mg-calcite and aragonite samples suggests that mineralogy is the first order control for the cation component, although the range present with each population indicates that additional factors are fractionating the cations. Mixing between seawater DIC and pore fluid DIC is unlikely to explain to explain the entire range of the variability seen in Ca isotopes because the difference in $\delta^{44}Ca$ values between seawater and porefluid is likely small over these depth ranges. In addition, fractionation during diffusion is small for aqueous Ca^{2+} (Bourg et al., 2010) and hydration/hydroxylation reactions do not apply to cations. Previous work (Teichert et al., 2005) has observed a 0.8‰ range in $\delta^{44}Ca$ in aragonitic MDACs in association with methane hydrates and speculated the range could be attributed to isotopic distillation of the surrounding pore-fluid due to the precipitation of aragonite enriched in ^{40}Ca. While precipitation of carbonate that is isotopically lighter than the fluid has the potential to elevate the pore fluid $\delta^{44}Ca$, such a large magnitude of enrichment would be hard to generate in such a shallow system in diffusive connection with bottom waters. Indeed, a later study (Teichert et al., 2009) that measured Ca isotopes in pore fluids in methane seep environments noted that MDAC precipitation only

increased the pore fluid profile by 0.1‰, making this unlikely to be the dominant mechanism for $\delta^{44}Ca$ enrichment in this setting. Additionally, a Rayleigh-style fractionation would not explain the Sr/Ca data, as we would expect Sr/Ca to increase with increasing $\delta^{44}Ca$ and increasing Rayleigh distillation. However, in our dataset, the Sr/Ca decreases with increasing $\delta^{44}Ca$ values.

Both laboratory experiments and studies of carbonate diagenesis in modern settings indicate that the partitioning of Sr and fractionation of Ca isotopes in inorganic carbonates depends on mineral precipitation rate. For the same fluid composition, higher Sr/Ca ratios and lower $\delta^{44}Ca$ values are associated with rapid precipitation rates whereas slow precipitation rates lead to low Sr/Ca ratios and higher $\delta^{44}Ca$ values (Lorens, 1981; Fantle and DePaolo, 2007; Tang et al., 2012; Nielsen et al., 2012) Although, the opposite effect (high precipitation rates show more positive calcium isotopes and lower Sr/Ca) has also been observed (Lemarchand et al., 2004; AlKhatib and Eisenhauer, 2017), these experiments were conducted with a more complex solution, and the observed differences may be due to changes in the aquacomplex binding to calcium. Also, our site location is at low temperatures (0-5°C), so we follow the more analogous experiments and assume that higher precipitation rates result in more negative calcium isotopes and higher Sr/Ca ratios.

Interpreted in this context, the highest $\delta^{44}Ca$ values and lowest Sr/Ca ratios in the MDACs reflect the slowest or closest to equilibrium precipitation rates whereas lower $\delta^{44}Ca$ values and high Sr/Ca ratios indicate significant KIEs. We note that the cavity filling aragonite cements has the lowest $\delta^{44}Ca$ values and also the highest (and therefore furthest from equilibrium) clumped isotope apparent temperatures and the largest Sr/Ca values. Therefore, it is possible that several geochemical properties of cavity filling aragonite cements can be attributed to kinetic effects associated with rapid precipitation. However, although the micritic aragonite cements have a similar range in $\delta^{44}Ca$ and Sr/Ca to the cavity filling aragonite cements, those from the Barents Sea are nearly invariant in clumped isotope apparent temperature and consistent with equilibrium at bottom water temperatures. This overlap in the Sr/Ca and $\delta^{44}Ca$ range in the aragonite cement and cavity filling aragonite cements despite differing behavior in clumped isotope apparent temperatures is a surprising feature of the dataset and implies that there are at least two different kinetic isotope effects operating on the MDACs, with different timescales and effects on carbon, oxygen, and calcium isotopes (and Sr/Ca ratios).

4.3 Proposed Explanation for Isotopic Patterns seen in Methane Seep Carbonates

We present a model of the mechanisms of MDAC precipitation that addresses our geochemical findings (Figure 7). We suggest there are two different timescales of kinetic isotope fractionation factors at play: KIE's that appear only at short time-scales (i.e., precipitation occurring within a few to tens of hours) when the rate of methane oxidation and/or DIC chemistry (i.e., dehydroxylation of HCO_3^-, outgassing of CO_2 or residues of diffusion) outstrips the rates of O, C and clumped isotope equilibration among the relevant species (e.g., between DIC and water), and a second, slower time-scale process when the rate of carbonate mineral precipitation exceeds the rate of Ca isotope equilibration between solids and solutions. These different processes appear to be coupled to generate kinetic isotope effects in some phases in all of the geochemical systems, whereas in other phases only one of these systems appears to generate disequilibrium effects. Specifically, we argue that the slowest mineral growth rates (precipitation on thousand year plus timescales, e.g., (Fantle and DePaolo, 2007; Jacobson and Holmden, 2008)) are easily long enough to permit isotopic equilibration among the DIC species and water, and are just long enough, or nearly long enough, to permit Ca isotope equilibration

between pore fluids and growing carbonates; this end member is represented by the highest $\delta^{44}Ca$ micritic Mg-calcite cements and equilibrium Δ_{47}-temperatures. At higher overall carbonate precipitation rates (precipitation between several days to thousand year timescales), a KIE associated with mineral growth leads to reduced $\delta^{44}Ca$ values, yet growth is not yet fast enough to outstrip equilibration of the DIC-water system; this intermediate case is represented by low-$\delta^{44}Ca$ Mg-calcite cements and some aragonite cements yielding bottom water clumped isotope temperatures. A similar signature is seen in a previous study (Zhang et al., 2019) which found equilibrium signatures in clumped isotope measurements of carbonate concretions, which tend to grow under slow AOM rates and deeper in the sediment column (Crémière et al., 2012). Finally, the fastest carbonate growth rates - very fast precipitation on the order of days or less, (e.g., (Affek, 2013; Clog et al., 2015) - lead to large Ca isotope KIEs, low $\delta^{44}Ca$ values and a failure of the DIC pool to achieve internal isotopic equilibrium, such that KIE's associated with methane oxidation and/or DIC chemistry lead to carbonate clumped isotope temperatures being higher than physical temperatures; this end member is represented by the cavity filling aragonite cements with low $\delta^{44}Ca$ values and higher than bottom water clumped isotope temperatures.

The cavity filling aragonite cements data in the Barents Sea has a V-like signature in plots of Δ_{47} vs $\delta^{18}O$ (Figure 4b) and a linear trend in plots of Δ_{47} vs $\delta^{13}C$. The apex of the V corresponds to what is expected if aragonite grows in isotope equilibrium at local bottom water conditions, while the tops of the V correspond to aragonite that grows from fluids that are 1.5‰ lighter and 1.5‰ heavier in $\delta^{18}O$, have disequilibrium clumped isotope compositions corresponding to ~20 °C and $\delta^{13}C$ values similar to CO_2 produced from AOM. We propose that there are two different types of pore waters that are interacting with seawater when aragonite cavity filling aragonite cements are precipitating. The DIC content of both fluids are highly influenced by degassed CO_2 and the residues of diffusion (giving it the high Δ_{47}-temperatures) and AOM-derived DIC (giving it the low $\delta^{13}C$ values), but one fluid has $\delta^{18}O$ values that are 1.5‰ lighter than seawater while the other has $\delta^{18}O$ values that are 1.5‰ heavier than seawater. This difference in $\delta^{18}O$ could be due to mixing of varying amounts of the AOM-derived DIC fluid with either heavier clathrate derived fluids or lighter meteoric glacial-derived water from the continental margin, lighter waters related to the dehydration of clay minerals, or lighter pore waters residual to clathrate formation.

4.4 Implications for Paleotemperature Reconstructions

We show that MDACs could be a promising tool for paleoceanography. Mg-calcite MDACs which are thought to grow slowly in low CH_4 flux environments record bottom water temperatures, meaning similarly to deep-sea corals, they can be used to create a U-series dated clumped isotope paleotemperature record of the ocean (Thiagarajan et al., 2014). MDACs form along continental margins along a range of depth environments from shallow to the deep water (Campbell, 2006) making them well suited for mixed layer, thermocline and deep ocean paleoceanography.

This finding is in contrast with micritic aragonite cements and aragonite cavity filling cements which grow under variable CH_4 flux environments and can occasionally record bottom water temperatures but frequently record much higher temperatures. These aragonitic cements could be used to reconstruct changes in sedimentary conditions, such as CH_4 efflux, over time.

5. CONCLUSIONS

We present the carbon, oxygen, calcium and clumped isotope data for MDACs in the Barents Sea and North Sea. We find that the clumped isotope composition of Mg-calcite cements record bottom water temperatures. This result indicates that clumped isotope thermometry in Mg-calcite cement is suitable for U-series based paleoclimate reconstructions.

We also find that micritic aragonite cements and aragonite cavity filling aragonite cements display both equilibrium and disequilibrium signatures in carbon, oxygen and clumped isotopes. Additionally, both micritic aragonite cements and cavity filling aragonite cements have a range in calcium isotope values much lighter than predicted equilibrium values. We propose that the range in calcium isotope variation can be explained by changes in the rate of calcification and mineralogy and that the range in Δ_{47}-temperatures can be explained by combined effects of those changes as well as changes in the residence time of DIC in the calcifying fluid. The warm Δ_{47}-temperatures are a result of intense CO_2 degassing or residues to CO_2 diffusion that can occur in high flux methane seep environments, producing residual HCO_3^- with a "warm" disequilibrium signature in clumped isotopes. When calcification rates are fast and DIC equilibration times are slow, that "warm" disequilibrium signature is incorporated into the carbonate as a hot Δ_{47} signature. However, if DIC equilibration occurs quickly then the "warm" disequilibrium signature equilibrates with DIC and the carbonates record an equilibrium Δ_{47}-temperature.

6. ACKNOWLEDGEMENTS

This work was supported by the Research Council of Norway through the Petromaks2 - NORCRUST project (grant number 255150).

7. REFERENCES

Aagaard-Sørensen S., Husum K., Hald M. and Knies J. (2010) Paleoceanographic development in the SW Barents Sea during the Late Weichselian–Early Holocene transition. *Quaternary Science Reviews* **29**, 3442–3456.

Affek H. P. (2013) Clumped isotopic equilibrium and the rate of isotope exchange between CO2 and water. *American Journal of Science* **313**, 309–325.

AlKhatib M. and Eisenhauer A. (2017) Calcium and strontium isotope fractionation in aqueous solutions as a function of temperature and reaction rate; I. Calcite. *Geochimica et Cosmochimica Acta* **209**, 296–319.

Aloisi G., Bouloubassi I., Heijs S. K., Pancost R. D., Pierre C., Sinninghe Damsté J. S., Gottschal J. C., Forney L. J. and Rouchy J.-M. (2002) CH4-consuming microorganisms and the formation of carbonate crusts at cold seeps. *Earth and Planetary Science Letters* **203**, 195–203.

Bayon G., Dupré S., Ponzevera E., Etoubleau J., Chéron S., Pierre C., Mascle J., Boetius A. and de Lange G. J. (2013) Formation of carbonate chimneys in the Mediterranean Sea linked to deep-water oxygen depletion. *Nature Geoscience* **6**, 755.

Boetius A., Ravenschlag K., Schubert C. J., Rickert D., Widdel F., Gieseke A., Amann R., Jørgensen B. B., Witte U. and Pfannkuche O. (2000) A marine microbial consortium apparently mediating anaerobic oxidation of methane. *Nature* **407**, 623.

Bohrmann G., Greinert J., Suess E. and Torres M. (1998) Authigenic carbonates from the Cascadia subduction zone and their relation to gas hydrate stability. *Geology* **26**, 647–650.

Bonifacie M., Calmels D., Eiler J. M., Horita J., Chaduteau C., Vasconcelos C., Agrinier P., Katz A., Passey B. H., Ferry J. M. and Bourrand J.-J. (2017) Calibration of the dolomite clumped isotope thermometer from 25 to 350 °C, and implications for a universal calibration for all (Ca, Mg, Fe)CO3 carbonates. *Geochimica et Cosmochimica Acta* **200**, 255–279.

Bourg I. C., Richter F. M., Christensen J. N. and Sposito G. (2010) Isotopic mass dependence of metal cation diffusion coefficients in liquid water. *Geochimica et Cosmochimica Acta* **74**, 2249–2256.

Brand W., Assonov and Coplen T. (2010) Correction for the 17O interference in δ(13C) measurements when analyzing CO2 with stable isotope mass spectrometry (IUPAC Technical Report). *pac* **82**, 1719.

Campbell K. A. (2006) Hydrocarbon seep and hydrothermal vent paleoenvironments and paleontology: Past developments and future research directions. *Palaeogeography, Palaeoclimatology, Palaeoecology* **232**, 362–407.

Clog M., Stolper D. and Eiler J. M. (2015) Kinetics of CO2(g)–H2O(1) isotopic exchange, including mass 47 isotopologues. *Chemical Geology* **395**, 1–10.

Crémière A., Chand S., Sahy D., Thorsnes T., Martma T., Noble S. R., Pedersen J. H., Brunstad H. and Lepland A. (2018) Structural controls on seepage of thermogenic and microbial methane since the last glacial maximum in the Harstad Basin, southwest Barents Sea. *Marine and Petroleum Geology* **98**, 569–581.

Crémière A., Lepland A., Chand S., Sahy D., Condon D. J., Noble S. R., Martma T., Thorsnes T., Sauer S. and Brunstad H. (2016a) Timescales of methane seepage on the Norwegian margin following collapse of the Scandinavian Ice Sheet. *Nature Communications* **7**, 11509.

Crémière A., Lepland A., Chand S., Sahy D., Kirsimäe K., Bau M., Whitehouse M. J., Noble S. R., Martma T., Thorsnes T. and Brunstad H. (2016b) Fluid source and methane-related diagenetic processes recorded in cold seep carbonates from the Alvheim channel, central North Sea. *Chemical Geology* **432**, 16–33.

Crémière A., Pierre C., Blanc-Valleron M.-M., Zitter T., Çağatay M. N. and Henry P. (2012) Methane-derived authigenic carbonates along the North Anatolian fault system in the Sea of Marmara (Turkey). *Deep Sea Research Part I: Oceanographic Research Papers* **66**, 114–130.

Cui H., Kaufman A. J., Xiao S., Zhou C. and Liu X.-M. (2017) Was the Ediacaran Shuram Excursion a globally synchronized early diagenetic event? Insights from methane-derived authigenic carbonates in the uppermost Doushantuo Formation, South China. *Chemical Geology* **450**, 59–80.

Daëron M., Blamart D., Peral M. and Affek H. P. (2016) Absolute isotopic abundance ratios and the accuracy of Δ47 measurements. *Chemical Geology* **442**, 83–96.

Davidson D. W., Leaist D. G. and Hesse R. (1983) Oxygen-18 enrichment in the water of a clathrate hydrate. *Geochimica et Cosmochimica Acta* **47**, 2293–2295.

Dennis K. J. and Schrag D. P. (2010) Clumped isotope thermometry of carbonatites as an indicator of diagenetic alteration. *Geochimica et Cosmochimica Acta* **74**, 4110–4122.

Devriendt L. S., Watkins J. M. and McGregor H. V. (2017) Oxygen isotope fractionation in the CaCO3-DIC-H2O system. *Geochimica et Cosmochimica Acta* **214**, 115–142.

Eagle R. A., Eiler J. M., Tripati A. K., Ries J. B., Freitas P. S., Hiebenthal C., Wanamaker Jr. A. D., Taviani M., Elliot M., Marenssi S., Nakamura K., Ramirez P. and Roy K. (2013) The influence of temperature and seawater carbonate saturation state on 13C–18O bond ordering in bivalve mollusks. *Biogeosciences* **10**, 4591–4606.

Eiler J. M. (2011) Paleoclimate reconstruction using carbonate clumped isotope thermometry. *Quaternary Science Reviews* **30**, 3575–3588.

Eiler J. M. and Schauble E. (2004) 18O13C16O in earth's atmosphere. *Geochimica et Cosmochimca Acta* **68**, 4767–4777.

Falk E. S., Guo W., Paukert A. N., Matter J. M., Mervine E. M. and Kelemen P. B. (2016) Controls on the stable isotope compositions of travertine from hyperalkaline springs in Oman: Insights from clumped isotope measurements. *Geochimica et Cosmochimica Acta* **192**, 1–28.

Fantle M. S. and DePaolo D. J. (2007) Ca isotopes in carbonate sediment and pore fluid from ODP Site 807A: The Ca2+(aq)–calcite equilibrium fractionation factor and calcite recrystallization rates in Pleistocene sediments. *Geochimica et Cosmochimica Acta* **71**, 2524–2546.

Gabitov R. I., Sadekov A. and Leinweber A. (2014) Crystal growth rate effect on Mg/Ca and Sr/Ca partitioning between calcite and fluid: An in situ approach. *Chemical Geology* **367**, 70–82.

Ghosh P., Adkins J. F., Affek H., Balta B., Guo W., Schauble E. A., Schrag D. P. and Eiler J. M. (2006) 13C-18O bonds in carbonate minerals: A new kind of paleothermometer. *Geochimica et Cosmochimca Acta* **70**, 1439–1456.

Han X., Suess E., Sahling H. and Wallmann K. (2004) Fluid venting activity on the Costa Rica margin: new results from authigenic carbonates. *International Journal of Earth Sciences* **93**, 596–611.

Heuser A. and Eisenhauer A. (2008) The Calcium Isotope Composition (δ44/40Ca) of NIST SRM 915b and NIST SRM 1486. *Geostandards and Geoanalytical Research* **32**, 311–315.

Hines S. K. V., Eiler J. M., Southon J. R. and Adkins J. F. (2019) Dynamic Intermediate Waters Across the Late Glacial Revealed by Paired Radiocarbon and Clumped Isotope Temperature Records. *Paleoceanography and Paleoclimatology* **34**, 1074–1091.

Huntington K. W., Eiler J. M., Affek H. P., Guo W., Bonifacie M., Yeung L. Y., Thiagarajan N., Passey B., Tripati A., Daëron M. and Came R. (2009) Methods and limitations of 'clumped' CO2 isotope (Δ47) analysis by gas-source isotope ratio mass spectrometry. *Journal of Mass Spectrometry* **44**, 1318–1329.

Jacobson A. D. and Holmden C. (2008) δ44Ca evolution in a carbonate aquifer and its bearing on the equilibrium isotope fractionation factor for calcite. *Earth and Planetary Science Letters* **270**, 349–353.

Kim S. T., Hillaire-Marcel C. and Mucci A. (2006) Mechanisms of equilibrium and kinetic oxygen isotope effects in synthetic aragonite at 25°. *Geochimica et Cosmochimca Acta* **70**, 5790–5801.

Kim S.-T., Mucci A. and Taylor B. E. (2007a) Phosphoric acid fractionation factors for calcite and aragonite between 25 and 75 °C: Revisited. *Chemical Geology* **246**, 135–146.

Kim S.-T. and O'Neil J. R. (1997) Temperature dependence of d18O. *Geochemica et Cosmochimica Acta* **61**, 3461–3475.

Kim S.-T., O'Neil J. R., Hillaire-Marcel C. and Mucci A. (2007b) Oxygen isotope fractionation between synthetic aragonite and water: Influence of temperature and Mg2+ concentration. *Geochimica et Cosmochimica Acta* **71**, 4704–4715.

Kvenvolden K. A. (1993) Gas hydrates—geological perspective and global change. *Reviews of Geophysics* **31**, 173–187.

Lemarchand D., Wasserburg G. J. and Papanastassiou D. A. (2004) Rate-controlled calcium isotope fractionation in synthetic calcite. *Geochimica et Cosmochimica Acta* **68**, 4665–4678.

Levitt N. P., Eiler J. M., Romanek C. S., Beard B. L., Xu H. and Johnson C. M. (2018) Near Equilibrium 13C□18O Bonding During Inorganic Calcite Precipitation Under Chemo-Stat Conditions. *Geochemistry, Geophysics, Geosystems* **19**, 901–920.

Lorens R. B. K.-. F. (1981) Sr, Cd, Mn, and Co distribution coefficients in calcite as a function of calcite precipitation rate. *Geochimica Cosmochimica Acta* **45**, 553–561.

Loyd S. J., Sample J., Tripati R. E., Defliese W. F., Brooks K., Hovland M., Torres M., Marlow J., Hancock L. G., Martin R., Lyons T. and Tripati A. E. (2016) Methane seep carbonates yield clumped isotope signatures out of equilibrium with formation temperatures. **7**, 12274.

McConnaughey T. (1989) 13C and 18O isotopic disequilibrium in biological carbonates: I. Patterns. *Geochimica et Cosmochimica Acta* **53**, 151–162.

McGlynn S. E., Chadwick G. L., Kempes C. P. and Orphan V. J. (2015) Single cell activity reveals direct electron transfer in methanotrophic consortia. *Nature* **526**, 531.

McRea J. M. (1950) On the isotopic chemistry of carbonates and a paleotemperature scale. *Journal of Chemical Physics* **18**, 849–857.

Nielsen L. C., DePaolo D. J. and De Yoreo J. J. (2012) Self-consistent ion-by-ion growth model for kinetic isotopic fractionation during calcite precipitation. *Geochimica et Cosmochimica Acta* **86**, 166–181.

O'Leary M. H. (1984) Measurement of the isotope fractionation associated with diffusion of carbon dioxide in aqueous solution. *The Journal of Physical Chemistry* **88**, 823–825.

Passey B. H., Levin N. E., Cerling T. E., Brown F. H. and Eiler J. M. (2010) High-temperature environments of human evolution in East Africa based on bond ordering in paleosol carbonates. *Proceedings of the National Academy of Sciences*. Available at: http://www.pnas.org/content/early/2010/06/07/1001824107.abstract.

Reeburgh W. S. (2007) Oceanic Methane Biogeochemistry. *Chem. Rev.* **107**, 486–513.

Römer M., Sahling H., Pape T., Bahr A., Feseker T., Wintersteller P. and Bohrmann G. (2012) Geological control and magnitude of methane ebullition from a high-flux seep area in the Black Sea—the Kerch seep area. *Marine Geology* **319–322**, 57–74.

Schauer A. J., Kelson J., Saenger C. and Huntington K. W. (2016) Choice of 17O correction affects clumped isotope (Δ47) values of CO2 measured with mass spectrometry. *Rapid Communications in Mass Spectrometry* **30**, 2607–2616.

Smrzka D., Kraemer S. M., Zwicker J., Birgel D., Fischer D., Kasten S., Goedert J. L. and Peckmann J. (2015) Constraining silica diagenesis in methane-seep deposits. *Palaeogeography, Palaeoclimatology, Palaeoecology* **420**, 13–26.

Staudigel P. T. and Swart P. K. (2018) A Kinetic Difference Between 12C- and 13C-Bound Oxygen Exchange Rates Results in Decoupled δ18O and Δ47 Values of Equilibrating DIC Solutions. *Geochemistry, Geophysics, Geosystems* **19**, 2371–2383.

Suess E. (2014) Marine cold seeps and their manifestations: geological control, biogeochemical criteria and environmental conditions. *International Journal of Earth Sciences* **103**, 1889–1916.

Tang J., Dietzel M., Fernandez A., Tripati A. K. and Rosenheim B. E. (2014) Evaluation of kinetic effects on clumped isotope fractionation (Δ47) during inorganic calcite precipitation. *Geochimica et Cosmochimica Acta* **134**, 120–136.

Tang J., Niedermayr A., Köhler S. J., Böhm F., Kısakürek B., Eisenhauer A. and Dietzel M. (2012) Sr2+/Ca2+ and 44Ca/40Ca fractionation during inorganic calcite formation: III. Impact of salinity/ionic strength. *Geochimica et Cosmochimica Acta* **77**, 432–443.

Tarutani T., Clayton R. N. and Mayeda T. K. (1969) The effect of polymorphism and magnesium substitution on oxygen isotope fractionation between calcium carbonate and water. *Geochimica et Cosmochimica Acta* **33**, 987–996.

Teichert B. M. A., Gussone N., Eisenhauer A. and Bohrmann G. (2005) Clathrites: Archives of near-seafloor pore-fluid evolution (δ44/40Ca, δ13C, δ18O) in gas hydrate environments. *Geology* **33**, 213–216.

Teichert B. M. A., Gussone N. and Torres M. E. (2009) Controls on calcium isotope fractionation in sedimentary porewaters. *Earth and Planetary Science Letters* **279**, 373–382.

Thiagarajan N., Adkins J. and Eiler J. (2011) Carbonate clumped isotope thermometry of deep-sea corals and implications for vital effects. *Geochimica Et Cosmochimica Acta* **75**, 4416–4425.

Thiagarajan N., Subhas A. V., Southon J. R., Eiler J. M. and Adkins J. F. (2014) Abrupt pre-Bølling–Allerød warming and circulation changes in the deep ocean. *Nature* **511**, 75.

Tripati A. K., Eagle R. A., Thiagarajan N., Gagnon A. C., Bauch H., Halloran P. R. and Eiler J. M. (2010) 13C–18O isotope signatures and 'clumped isotope' thermometry in foraminifera and coccoliths. *Geochimica Et Cosmochimica Acta* **74**, 5697–5717.

Uchikawa J. and Zeebe R. E. (2012) The effect of carbonic anhydrase on the kinetics and equilibrium of the oxygen isotope exchange in the CO2–H2O system: Implications for δ18O vital effects in biogenic carbonates. *Geochimica et Cosmochimica Acta* **95**, 15–34.

Usdowski E., Michaelis J., Bottcher M. E. and Hoefs J. (1991) Factors for the oxygen isotope equilibrium fractionation between aqueous and gaseous CO2, carbonic acid, bicarbonate, carbonate, and water (19°C). *Zeitschrift fur Physikalische Chemie* **170**, 237–249.

Wacker U., Fiebig J., Tödter J., Schöne B. R., Bahr A., Friedrich O., Tütken T., Gischler E. and Joachimski M. M. (2014) Empirical calibration of the clumped isotope paleothermometer using calcites of various origins. *Geochimica et Cosmochimica Acta* **141**, 127–144.

Watkins J. M. and Hunt J. D. (2015) A process-based model for non-equilibrium clumped isotope effects in carbonates. *Earth and Planetary Science Letters* **432**, 152–165.

Whiticar M. J. (1999) Carbon and hydrogen isotope systematics of bacterial formation and oxidation of methane. *Chemical Geology* **161**, 291–314.

Wolf-Gladrow D. and Zeebe R. E. (2001) *CO2 in seawater: equilibrium, kinetics, isotopes*., Elsevier, Amsterdam.

Zeebe R. (1999) An explanation of the effect of seawater carbonate concentration on foraminiferal oxygen isotopes. *Geochimica et Cosmochimica Acta* **63**, 2001–2007.

Zhang N., Lin M., Snyder G. T., Kakizaki Y., Yamada K., Yoshida N. and Matsumoto R. (2019) Clumped isotope signatures of methane-derived authigenic carbonate presenting equilibrium values of their formation temperatures. *Earth and Planetary Science Letters* **512**, 207–213.

FIGURE CAPTIONS

Fig. 1. A map of our study location. Samples were collected via ROV from the Barents and North Sea.

Fig. 2. Scanning electron microscope images of cavity filling aragonite cements (A), micritic aragonite cement (B) and micritic Mg-calcite cements (C). A diagram of methane seep formation documenting important processes at play for MDAC formation. Micritic Mg-calcite cements tend to occur deeper in the sediment column, but can be exposed at the surface due to erosion. Micritic Mg-calcite cements tend to occur under low CH_4 flux environments, while micritic aragonite cements tend to form under high CH_4 flux environments. The cements form a loosely consolidated structure, which under higher CH_4 flow conditions can be flushed out to

form cavities. As more methane travels through the cavities, AOM activity can be renewed, and a purer cavity filling aragonite cements forms within the cavities.

Fig. 3. Crossplots of Δ_{47}-temperature (error bars are 1σ) vs % Mg-calcite as determined by X-ray diffraction for the Barents Sea (A) and North Sea (B). Micritic Mg-calcite cements in both locations consistently record bottom water temperature within 2σ, while micritic aragonite cements and cavity filling aragonite cements record a range of temperatures. One sample has a Mg-calcite content of 24%. We think this sample likely reflects a mixture of aragonite and Mg-calcite.

Fig. 4. Crossplots of Temperature (error bars are 1σ) vs $\delta^{18}O$ (A, D), Temperature vs $\delta^{13}C$ (B, E) and $\delta^{18}O$ vs $\delta^{13}C$ (C, F). A-C are for the Barents Sea while, D-F are for the North Sea. The grey dots are previous $\delta^{18}O$ and $\delta^{13}C$ measurements made on MDACs from the Barents Sea (Crémière et al., 2016a). Micritic Mg-calcite cements in both locations consistently record bottom water temperature within 2σ, while micritic aragonite cements and cavity filling aragonite cements record a range of temperatures.

Fig. 5. Crossplots of Temperature (error bars are 1σ) vs $\delta^{44}Ca$ (A, E), $\delta^{18}O$ vs $\delta^{44}Ca$ (B, F), $\delta^{13}C$ vs $\delta^{44}Ca$ (C, G) and Sr/Ca vs $\delta^{44}Ca$ (D, H). A-D are for the Barents Sea while, E-F are for the North Sea. Micritic Mg-calcite cements in both locations consistently record bottom water temperature within 2σ, while micritic aragonite cements and cavity filling aragonite cements record a range of temperatures.

Fig. 6. Crossplot of $\Delta_{47,measured}$- $\Delta_{47,expected}$ vs $\delta^{18}O_{measured}$-$\delta^{18}O_{expected}$ for the Holocene (A) and deglacial (B) Barents Sea samples as well as Holocene North Sea samples (C). The values used to calculate $\Delta_{47,expected}$ and $\delta^{18}O_{expected}$ are discussed in the text in section 4.1. The origin reflects the value expected if the MDAC had grown in equilibrium with seawater. Also shown are deviations expected for CO_2 hydration/hydroxylation, diffusion, variation in pH, mixing between seawater and AOM-derived DIC as well as the output of Watkins' model (Watkins and Hunt, 2015) where pH, and rate are varied across a range of values. We find that variations in $\delta^{18}O$ and Δ_{47} in the MDACs are consistent with being affected by pH, mixing, the residues of CO_2 diffusion and CO_2 degassing. Note that at these temperatures, a 0.01‰ change in Δ_{47} corresponds to 2°C.

Fig. 7. A schematic showing how AOM-derived DIC, CO_2 degassing, DIC equilibration, and various waters together affect the final composition of the MDAC. There are two different timescales of kinetic isotope fractionation factors at play: KIE's that appear only at short time-scales (i.e., precipitation occurring within a few to tens of hours) when the rate of methane oxidation and/or DIC chemistry (i.e., dehydroxylation of HCO_3^-, outgassing of CO_2 or residues of diffusion) outstrips the rates of O, C and clumped isotope equilibration among the relevant species (e.g., between DIC and water), and a second, slower time-scale process when the rate of carbonate mineral precipitation exceeds the rate of Ca isotope equilibration between solids and solutions.

Supplementary Figures and Tables

SI Figure 1-Photographs of MDACs showing where each stable and clumped isotope as well as XRD measurement was made. All of the MDAC offcuts are ~5x5 cm except for the P120020 Pistol and Rabbit offcuts which are ~2x2cm.

SI Table 1-Stable and Clumped Isotope Meausurements of MDACs

SI Table 2-Stable and Clumped Isotope Measurements made of Heated and Equilibrated Gases during MDAC measurements

SI Table 3-Stable and Clumped Isotope Measurements made of Standards during MDAC measurements

SI-Table 4-XRD, Ca isotope and Sr/Ca measurements made of MDACs.

Declaration of interests

☒ The authors declare that they have no known competing financial interests or personal relationships that could have appeared to influence the work reported in this paper.

☐The authors declare the following financial interests/personal relationships which may be considered as potential competing interests:

FIgure 1

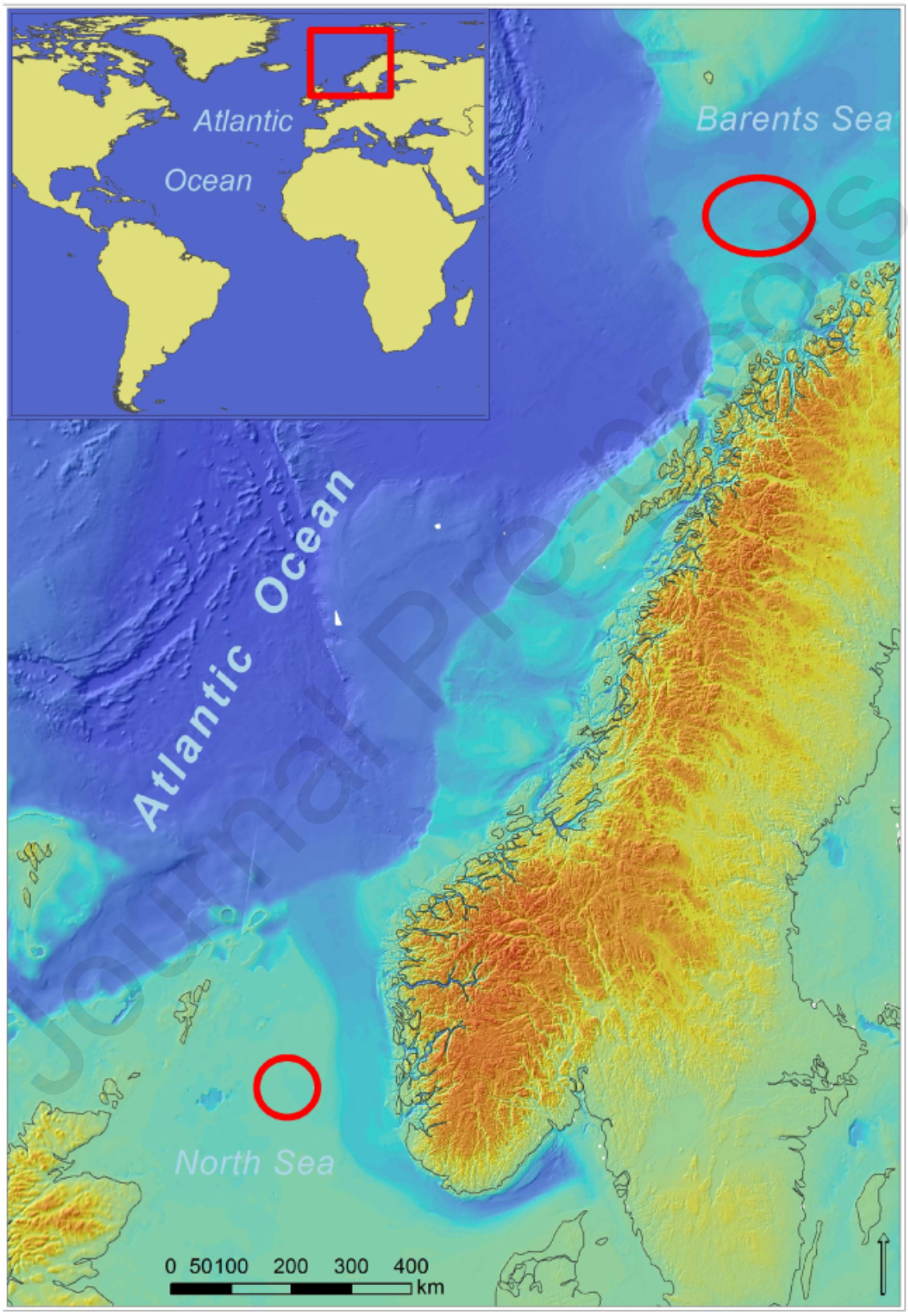

Figure 2

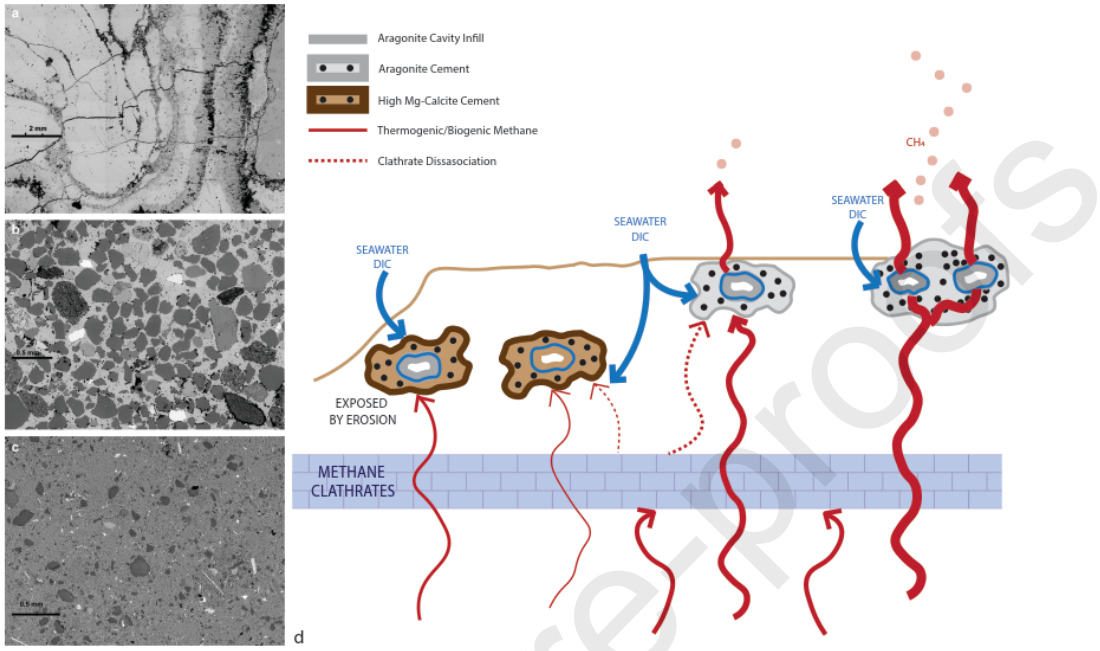

Figure 3

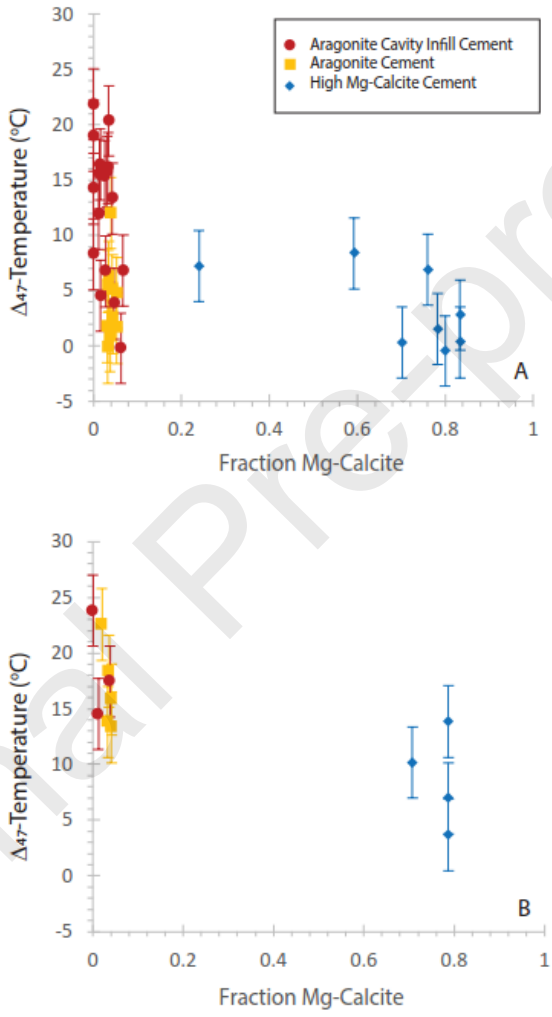

Figure 4

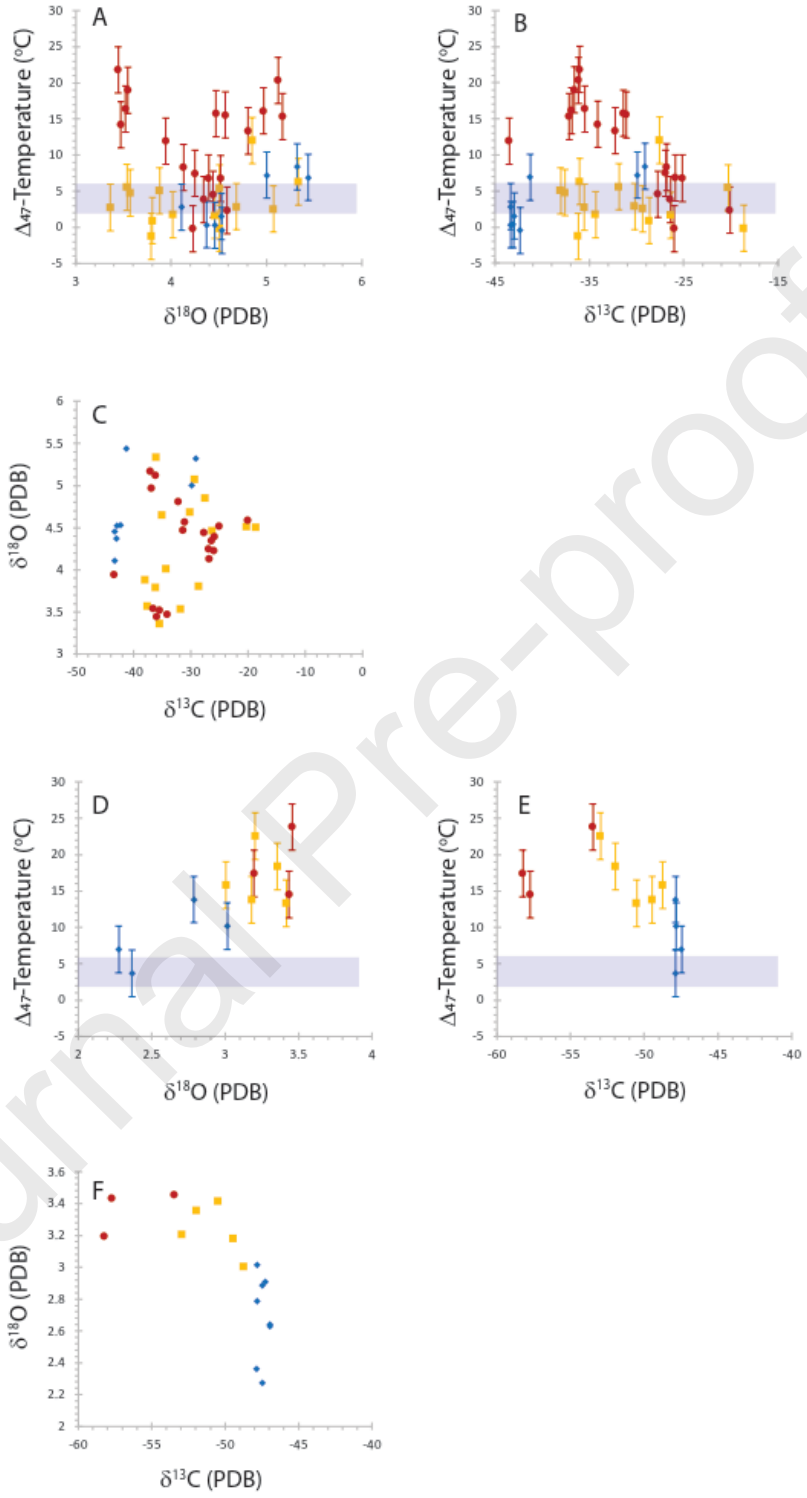

Figure 5

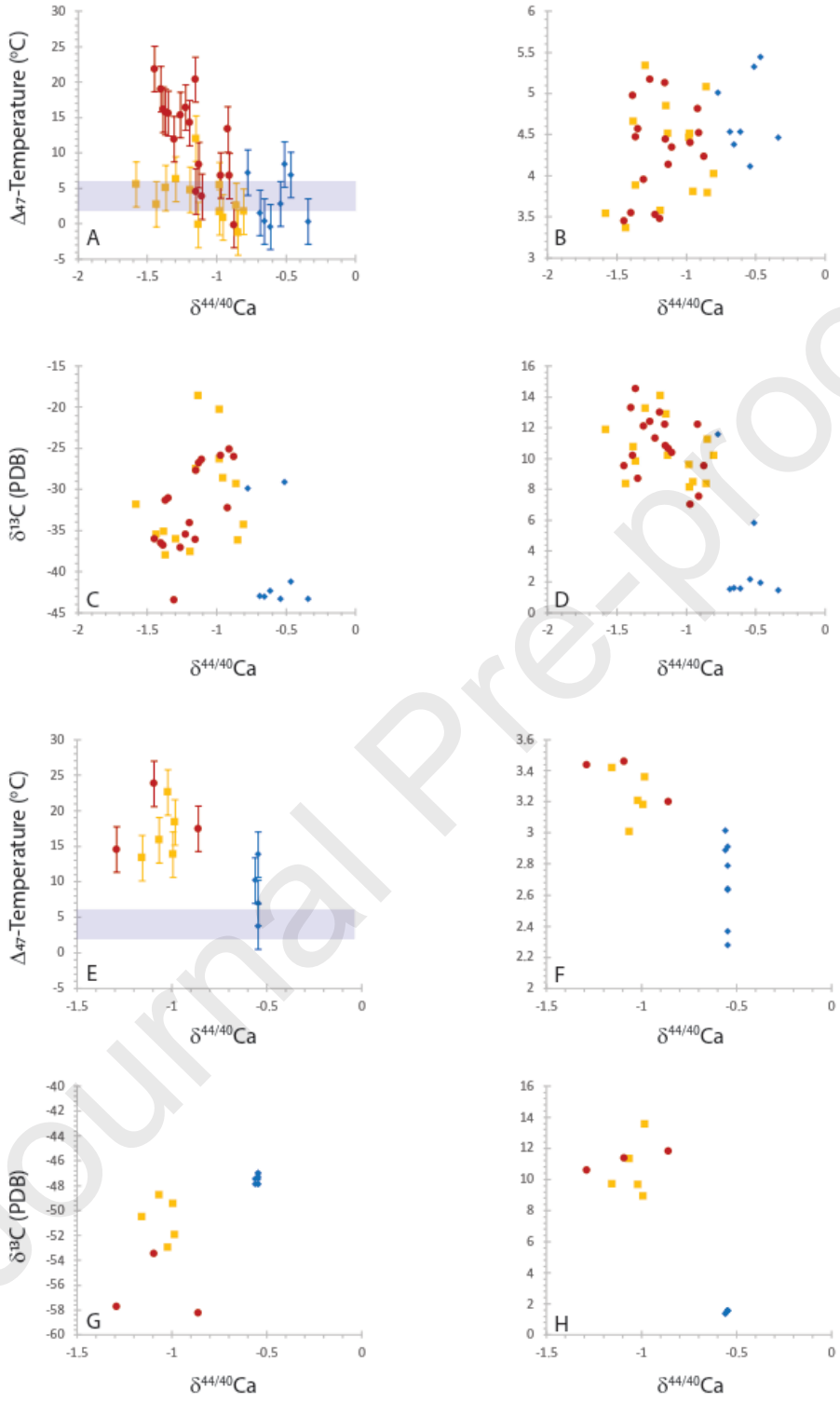

Figure 6

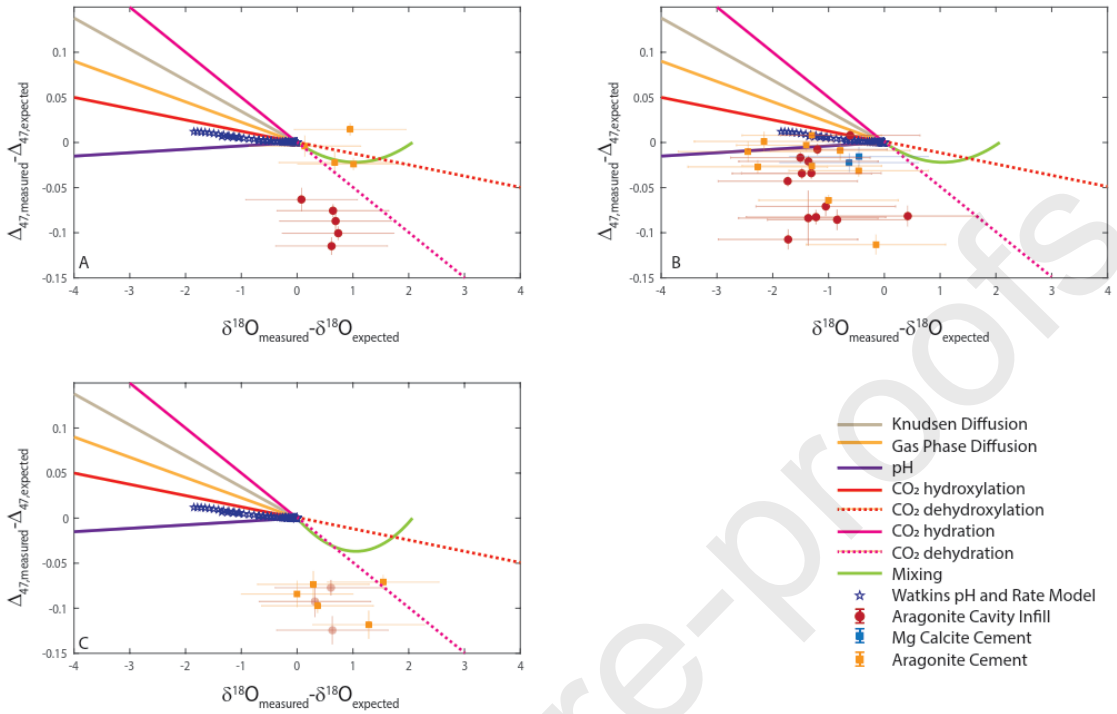

Figure 7